



Processing maps for the Cu-Cr-Zr-Y alloy hot deformation behavior

Yi Zhang^{a,d,*}, Zhe Chai^{a,d}, Alex A. Volinsky^{b,*}, Baohong Tian^{a,d}, Huili Sun^{a,d}, Ping Liu^c, Yong Liu^{a,d}

^a College of Materials Science and Engineering, Henan University of Science and Technology, Luoyang 471003, China

^b Department of Mechanical Engineering, University of South Florida, Tampa 33620, USA

^c College of Materials Science and Engineering, University of Shanghai for Science and Technology, Shanghai 200093, China

^d Collaborative Innovation Center of Nonferrous Metals, Henan Province, Luoyang 471003, China

ARTICLE INFO

Article history:

Received 14 October 2015

Received in revised form

22 January 2016

Accepted 6 March 2016

Available online 8 March 2016

Keywords:

Cu-Cr-Zr-Y alloys

Hot deformation behavior

Constitutive equation

Processing map.

ABSTRACT

Hot deformation behavior of the Cu-Cr-Zr-Y alloy was studied by hot compressive tests in the 650–850 °C temperature and 0.001–10 s⁻¹ strain rate ranges using the Gleeble-1500D thermo-mechanical simulator. The flow stress behavior and microstructure evolution were observed during the hot deformation process. The peak stress increases with decreasing temperature and increasing strain rate. The apparent activation energy for hot deformation of the alloy is 336 kJ/mol. Based on the dynamic material model, the processing maps for the alloy were obtained at 0.3, 0.4 and 0.5 strain. The evolution of dynamic recrystallization microstructure strongly depends on the deformation temperature and strain rate. Dynamic recovery is the main softening mechanism at low temperature and high strain rate. Dynamic recrystallization appears at high temperatures and low strain rates. The precipitates of chromium-rich particles were observed during hot deformation. The addition of Y can refine the grain and effectively improve the hot workability of the Cu-Cr-Zr alloy. According to the processing maps and microstructure observations, the optimal hot working parameters for the Cu-Cr-Zr-Y alloy are 800–850 °C temperature range and 0.01–1 s⁻¹ strain rate range.

© 2016 Elsevier B.V. All rights reserved.

1. Introduction

The lead frame is one of the important parts of the integrated circuit. Due to the excellent mechanical and physical properties, copper alloys have been widely used as lead frame materials [1–4]. Typical copper alloys for the lead frame are Cu-Cr-Zr, Cu-Fe-P and Cu-Ni-Si alloys. Multiple studies have focused on improving the alloy strength and conductivity [5,6]. However, the hot workability is also very important for the alloys. Many investigations of the hot deformation processing for these alloys have been carried out. Li et al. [7] studied the Cu-8.0Ni-1.8Si-0.15Mg alloy and found that the work hardening, the dynamic recovery and recrystallization play important roles in affecting the plastic deformation behavior of the alloy in different temperature regions. Zhang et al. [8] found that the addition of Ce can improve the Cu-Cr-Zr alloy deformation activation energy during hot deformation. Zhang et al. [9] found that the increase of deformation activation energy of the Cu-Fe-P alloys is due to the existence of the Fe-rich particles, which act as obstacles for the dislocations movement, and lead to an increase of

the flow stress. A good understanding of hot deformation behavior and processing maps is very important for the copper alloys forming processes [10–13].

In this paper, the hot deformation behavior of the Cu-Cr-Zr-Y alloys has been investigated by hot compression tests. The constitutive equations and hot deformation activation energy for the alloy have been determined. The processing maps based on the dynamic material model (DMM) were derived to analyze the instability region and optimize the hot working parameters. The effects of deformation temperature and strain rate on the microstructure evolution of the alloy are also discussed.

2. Experimental details

The chemical composition (wt%) of the Cu-Cr-Zr-Y alloy is as follows: 0.4 Cr, 0.1 Zr, 0.05 Y and Cu balance. The alloy was melted in a vacuum induction furnace in argon, and then cast into a low carbon steel mold with Φ 83 mm \times 150 mm dimensions. The ingot was homogenized at 930 °C for 2 h. Subsequently, the ingot was forged into 25 mm diameter bars. Finally, the forged bars were solution-treated at 900 °C for 1 h, followed by water quenching.

The compression specimens were cut into a cylindrical shape with a diameter of 8 mm and height of 12 mm. The specimens

* Corresponding authors.

E-mail addresses: zhshgu436@163.com (Y. Zhang), volinsky@usf.edu (A.A. Volinsky).

were compressed at a strain rate of $0.001\text{--}10\text{ s}^{-1}$ and deformation temperature of $650\text{--}850\text{ }^{\circ}\text{C}$ using the Gleeble-1500D thermo-mechanical simulator. The specimens were heated to the deformation temperature at $5\text{ }^{\circ}\text{C/s}$ heating rate. Before deformation all specimens were held for 180 s to obtain uniform microstructure. All specimens were compressed to a true strain of 0.6 and immediately water-quenched from the test temperature. The deformed specimens were sectioned parallel to the compression axis. All specimens were polished and then etched with a solution of FeCl_3 (5 g) + $\text{C}_2\text{H}_5\text{OH}$ (85 mL) + HCl (10 mL). The microstructure was observed using OLYMPUS PMG3 optical microscope. Transmission electron microscopy (TEM) samples were prepared using Gatan 691 ion beam thinner. The precipitated phase was characterized using JEM-2100 (Joel, Japan) high resolution transmission electron microscope (HRTEM).

3. Results and discussion

3.1. Flow stress behavior

The true stress-true strain curves obtained for the Cu-Cr-Zr-Y alloy at various strain rates and deformation temperatures are shown in Fig. 1. It can be seen that the flow stress is strongly dependent on the deformation temperature and the strain rate. The flow stress increases with the strain rate and decreases with the deformation temperature. According to Fig. 1(a), the flow stress increases to a maximum and then decreases to a steady

state value when the alloy was deformed at $850\text{ }^{\circ}\text{C}$. This phenomenon is characteristic for hot working accompanied by dynamic recrystallization (DRX) [14]. Similar DRX behavior was observed at the deformation temperatures of $850\text{ }^{\circ}\text{C}$ under the strain rates of 0.1 s^{-1} and 1 s^{-1} , respectively. Typical continuous strain hardening was observed at the deformation temperature of $650\text{ }^{\circ}\text{C}$ in Fig. 1. The flow stress curve shows typical dynamic recovery (DRV) behavior at lower temperatures and higher strain rates. The main reason for this behavior is that the work hardening effect is stronger than the dynamic softening.

The variations in the peak stress (σ_p) at various temperatures and strain rates are shown in Fig. 2. It can be seen that the peak stress increases along with the strain rate at a given temperature. The peak stress decreases with the deformation temperature at a given strain rate.

3.2. Activation energy and constitutive equations

The constitutive equations are widely used to predict and analyze the relationship between the flow stress, strain rate and deformation temperature. The effects of temperature, strain rate and activation energy during hot deformation can be represented by the Zener-Hollomon Z parameter. All corresponding equations can be expressed as follows [15–17]:

$$\dot{\epsilon} = A_1 \sigma^{n_1} \exp\left(-\frac{Q}{RT}\right) \quad (1)$$

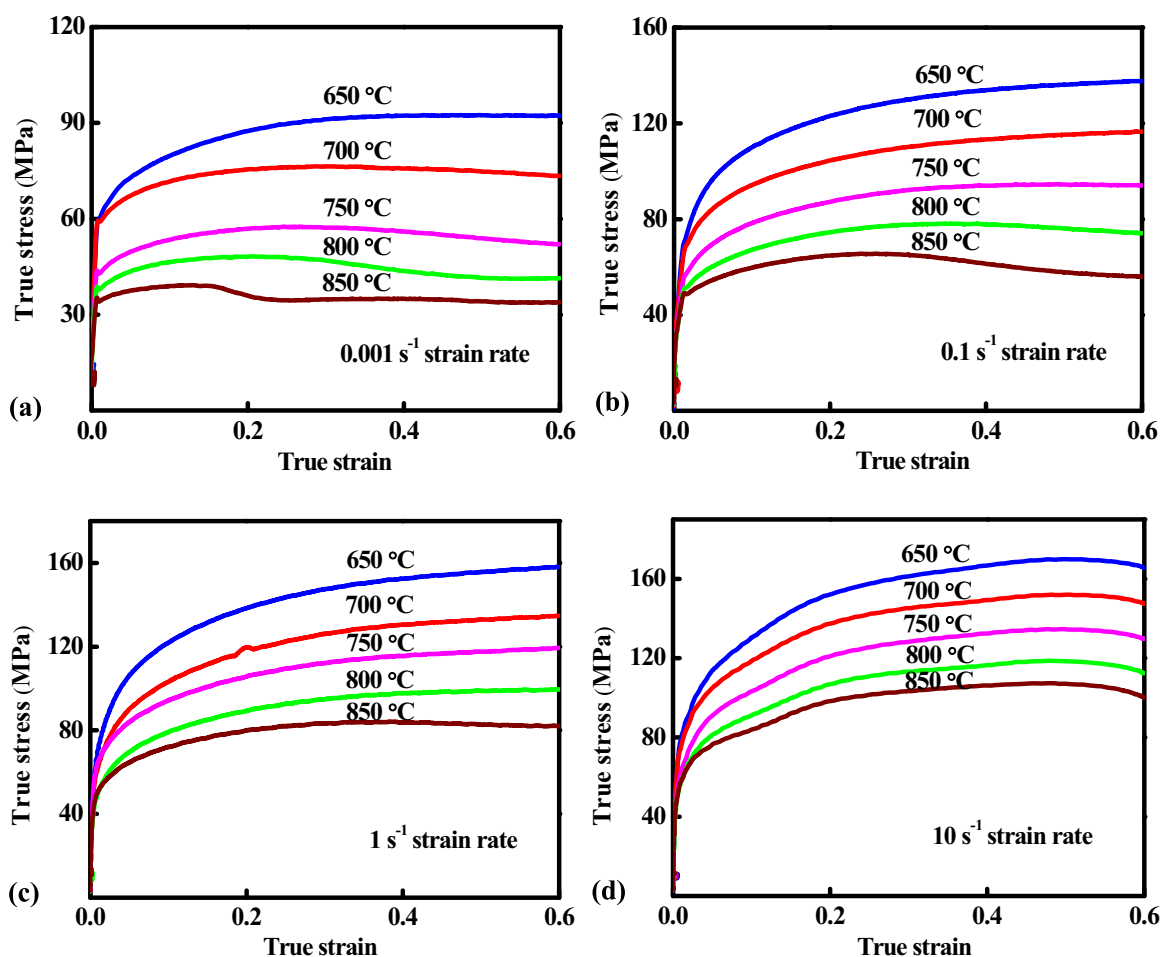


Fig. 1. True stress-strain curves of the Cu-Cr-Zr-Y alloy under different deformation temperatures with strain rates of: (a) $\dot{\epsilon}=0.001\text{ s}^{-1}$; (b) $\dot{\epsilon}=0.1\text{ s}^{-1}$; (c) $\dot{\epsilon}=1\text{ s}^{-1}$ and (d) $\dot{\epsilon}=10\text{ s}^{-1}$.

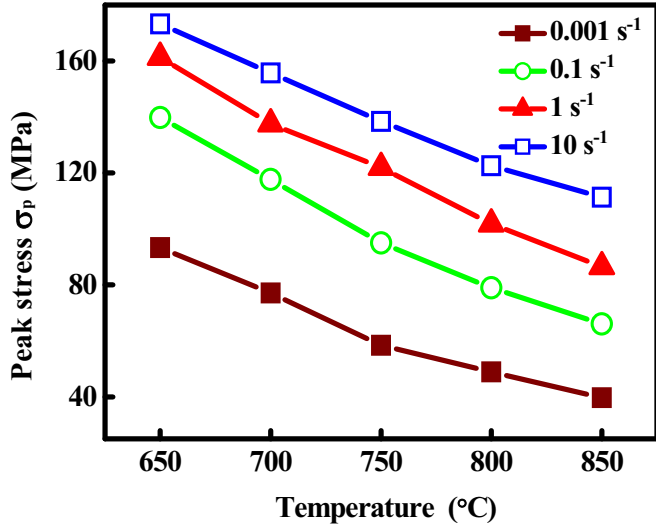


Fig. 2. Peak stress of the true stress-strain curves for the Cu-Cr-Zr-Y alloy under different deformation conditions.

$$\dot{\epsilon} = A_2 \exp(\beta\sigma) \exp\left(-\frac{Q}{RT}\right) \quad (2)$$

$$\dot{\epsilon} = A [\sinh(\alpha\sigma)]^n \exp\left(-\frac{Q}{RT}\right) \quad (3)$$

$$Z = \dot{\epsilon} \exp\left(\frac{Q}{RT}\right) \quad (4)$$

Here, $\dot{\epsilon}$ is the strain rate (s^{-1}), Q is the activation energy of DRX (kJ/mol), R is the universal gas constant ($8.314 \text{ J mol}^{-1} \text{ K}^{-1}$), T is the absolute temperature (K), σ is the flow stress (MPa) for a given strain, A (s^{-1}), A_1 , A_2 , n_1 , n and α (MPa^{-1}) are the materials constants ($\alpha = \beta/n_1$). Taking natural logarithms of both sides of (Eqs. (1) and 2) yields:

$$\ln \sigma = \frac{\ln \dot{\epsilon}}{n_1} - \frac{\ln A_1}{n_1} - \frac{Q}{n_1 RT} \quad (5)$$

$$\sigma = \frac{\ln \dot{\epsilon}}{\beta} - \frac{\ln A_2}{\beta} + \frac{Q}{\beta RT} \quad (6)$$

The values of n_1 and β can be determined from the slope of the linear regression lines in Fig. 3(a) and (b) ($\ln \dot{\epsilon} - \ln \sigma$ and $\ln \dot{\epsilon} - \sigma$). The corresponding values of n_1 and β are: $n_1 = 7.122$, $\beta = 0.0997$. Thus, the α value of the alloy is calculated as $\alpha = \beta/n_1 = 0.014 \text{ MPa}^{-1}$.

Taking natural logarithms of both sides of Eq. (3) yields:

$$\ln[\sinh(\alpha\sigma)] = \frac{1}{n} \ln \dot{\epsilon} + \frac{Q}{nR} \left(\frac{1}{T}\right) - \frac{1}{n} \ln A \quad (7)$$

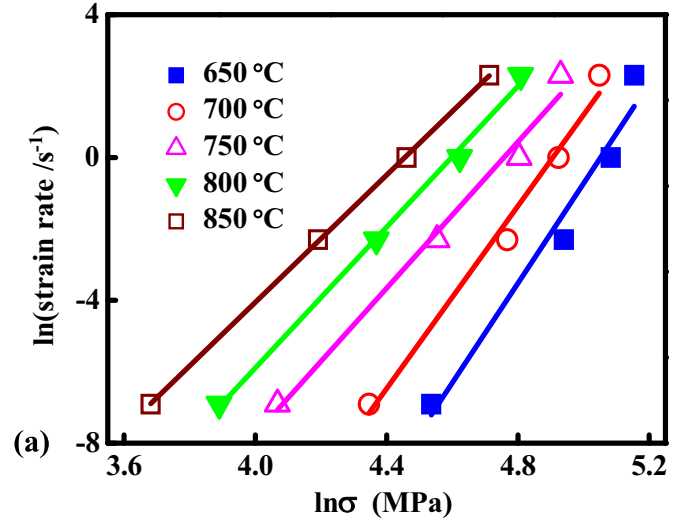
If $\dot{\epsilon}$ is a constant, Eq. (7) can be expressed as:

$$Q = R \left[\frac{\partial(\ln \dot{\epsilon})}{\partial \ln[\sinh(\alpha\sigma)]} \right]_T \left[\frac{\partial \ln[\sinh(\alpha\sigma)]}{\partial(1/T)} \right]_{\dot{\epsilon}} = RnS \quad (8)$$

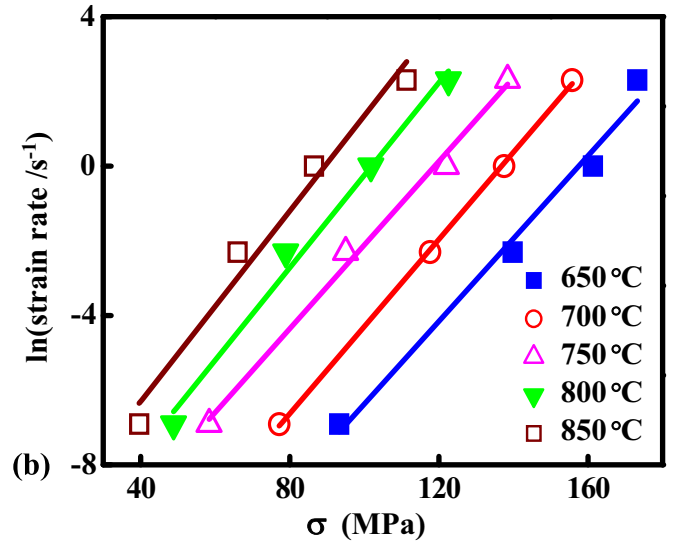
By plotting $\ln \dot{\epsilon} - \ln[\sinh(\alpha\sigma)]$ and $\ln[\sinh(\alpha\sigma)] - 1/T$ at different temperatures, the value of n and S can be calculated from the slope of the linear regression lines, as shown in Fig. 4(a) and (b). Consequently, the value of Q for the experimental alloy is $Q = RnS = 336 \text{ kJ/mol}$.

Taking natural logarithms of both sides of Eq. (4) yields:

$$\ln Z = \ln A + n \ln[\sinh(\alpha\sigma)] \quad (9)$$



(a)



(b)

Fig. 3. Relationships between: (a) $\ln \dot{\epsilon}$ and $\ln \sigma$; (b) $\ln \dot{\epsilon}$ and σ .

Fig. 5 illustrates the relationship between $\ln[\sinh(\alpha\sigma)]$ and $\ln Z$ for the Cu-Cr-Zr-Y alloy. The value of A can be obtained from the slope of the $\ln[\sinh(\alpha\sigma)] - \ln Z$, as shown in Fig. 5. The value of A is 1.723×10^{14} . Thus, the constitutive equation of the Cu-Cr-Zr-Y alloy in the hyperbolic-sine function can be expressed as:

$$\dot{\epsilon} = 1.723 \times 10^{14} [\sinh(0.0143\sigma)]^{7.122} \exp(-335.99/RT) \quad (10)$$

The Q value of this alloy is a little lower than that of the Cu-0.4Cr-0.1Zr alloy (392.5 kJ/mol), Cu-0.6Cr-0.03Zr alloy (572 kJ/mol) and the Cu-0.36Cr-0.03Zr alloy (432.6 kJ/mol), compared with references [8,18,19], respectively. The Q value reflects the level of an energy barrier for atoms diffusion during hot deformation, and the higher the activation energy Q , the harder the plastic deformation is [20]. Compared with the Cu-0.4Cr-0.1Zr alloy, the grains of the Cu-Cr-Zr alloy are also refined by the addition of Y, as shown in Fig. 10. Due to the refinement effect of Y addition, the DRX nucleation is improved by the increase of boundary area. Thus, more energy is accumulated accompanied by higher dislocation density with the Y addition. Therefore, the accumulated energy and higher dislocation density provide additional driving force for recrystallized nucleation. This indicates that dislocation movement and DRX are easier to occur for this experimental alloy, and the addition of Y can refine the grains and improve the dynamic

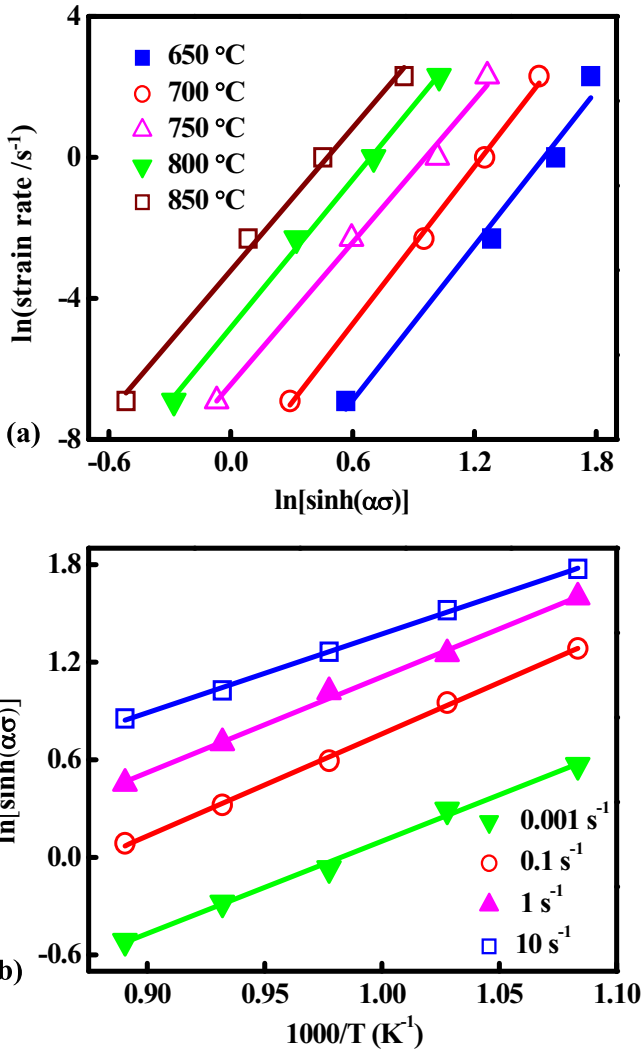


Fig. 4. Relationship between: (a) $\ln[\sinh(\alpha\sigma)]$ and $\ln\dot{\epsilon}$; (b) $\ln[\sinh(\alpha\sigma)]$ and $1000/T$.

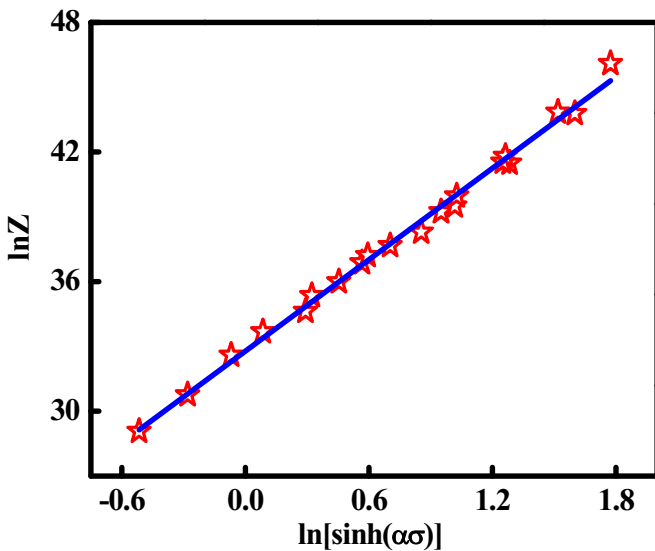


Fig. 5. The Zener-Hollomon parameter, Z , as a function of the flow stress.

recrystallization of the Cu-Cr-Zr alloy. The alloying element plays an important role in increasing the activation energy. Higher Cr and Zr alloying elements content in the Cu-0.6Cr-0.03Zr alloy

compared with the Cu-0.4Cr-0.1Zr-0.05Y alloy in reference [18], gives rise to much higher activation energy, possibly due to solution strengthening caused by these alloying elements. A higher strain rate (20 s^{-1}) was studied in reference [19]. If the strain rate is too high, there is not enough time for DRX, so a much higher activation energy Q is required. Finally, this indicates that the Cu-Cr-Zr-Y alloy has good hot workability.

3.3. Processing maps

The processing maps have been widely used to optimize the hot deformation processes. The dynamic material mode developed by Prasad et al. [20] was established based on the continuum mechanics and irreversible thermodynamics theories. In this model, the hot deformation process was considered to be an energy system and the workpiece was an energy dissipater under hot deformation [21,22]. The energy input in the workpiece was dissipated through the following two complementary parts during plastic deformation: G and J , defined as:

$$P = J + G = \sigma \dot{\epsilon} = \int_0^{\sigma} \dot{\epsilon} d\sigma + \int_0^{\dot{\epsilon}} \sigma d\dot{\epsilon} \tag{11}$$

In this model, G and J can be determined by the parameter m (the strain rate sensitivity index). The parameter m can be expressed as [23]:

$$\left(\frac{\partial J}{\partial G} \right)_{\epsilon, T} = \frac{\partial P}{\partial G} \frac{\partial J}{\partial P} = \frac{\sigma \dot{\epsilon}}{\dot{\epsilon} d\sigma} = \left[\frac{\partial(\ln \sigma)}{\partial(\ln \dot{\epsilon})} \right]_{\epsilon, T} = m \tag{12}$$

For an ideal linear dissipation process $m=1$ and $J=J_{\max} = \sigma \dot{\epsilon} / 2 = P/2$, and the efficiency of energy dissipation, η , which is defined as [24]:

$$\eta = \frac{J}{J_{\max}} = \frac{2m}{m + 1} \tag{13}$$

The instability map is developed based on the extremum principles of irreversible thermodynamics applied for large plastic flow body [25]. Thus, the flow instabilities can be defined by the instability parameter:

$$\xi(\dot{\epsilon}) = \frac{\partial \ln\left(\frac{m}{m+1}\right)}{\partial \ln \dot{\epsilon}} + m < 0 \tag{14}$$

The variation of the instability parameter $\xi(\dot{\epsilon})$ as a function of temperature and strain rate can be expressed by the instability map.

The processing maps of the Cu-Cr-Zr-Y alloy deformed at the strain of 0.3 and 0.5 are shown in Fig. 6(a) and (b), respectively. According to Fig. 6, the unstable region is represented by the shaded domains and the contour lines express the efficiency of energy dissipation. It can be seen that the distribution characteristics of the energy dissipation are similar, but the shaded domains increase with the strain. In all figures, a similar shaded domain was observed at the deformation temperature of 820–850 °C when the strain was 0.3. As seen in Fig. 6(a), the flow instability regions mostly consist of the three parts, one is in the low temperature-low strain rate region, and the other two are in the high temperature regions. According to Fig. 6(b), it can be seen that the flow domains were obtained over the entire testing temperature range at the strain rate below 0.1 s^{-1} . The value of η increased slightly with the strain for the same conditions. At the temperature range of 800–850 °C and the strain rate range of $0.001\text{--}0.1 \text{ s}^{-1}$, the spacing between the contour lines becomes closer. This shows that the η value strongly depends on the temperature and the strain rate. Meanwhile, the maximum η was obtained at the temperature range of 800–850 °C and the strain rate range of

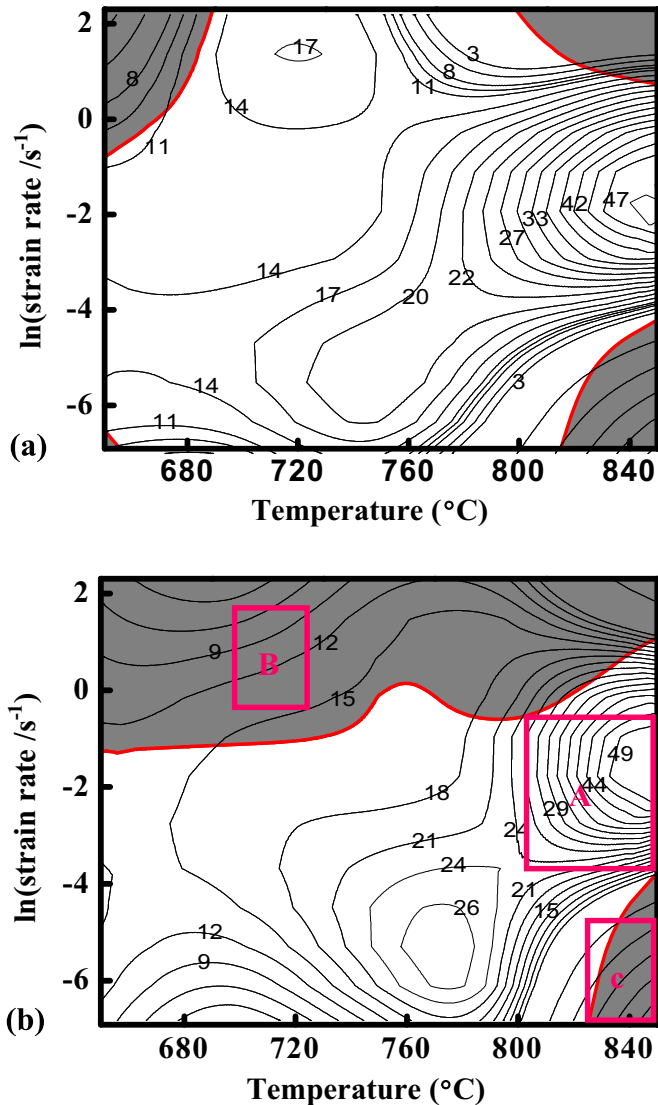


Fig. 6. Processing maps for the Cu-Cr-Zr-Y alloy at a true strain of: (a) 0.3 and (b) 0.5.

0.001–0.1 s^{-1} , which represent the optimal processing window. At the strain of 0.5, the maps exhibit three domains. Domain A in Fig. 6(b) represents a stable region with a peak efficiency of power dissipation, corresponding to the samples deformed at higher temperatures and lower strain rates. It revealed a greater efficiency of power dissipation in the temperature range of 800–850 °C and the strain rate range of 0.01–1 s^{-1} , with a peak efficiency of about 47% at 840 °C and 0.01 s^{-1} . The η value is higher and the workability is better in this deformation domain. This demonstrates that the material deformed at these conditions with high efficiency of power dissipation shows good workability [26]. Domain B occurs in the temperature range of 650–850 °C and the strain rate range of 1–10 s^{-1} . This region is at the lower temperature and higher strain rate conditions. Some very low values of power dissipation efficiency were observed, often considered as an instability region. Surrounding solute atoms easily form high density dislocations areas when deformed at high strain rate [27]. At the same time, the lattices distort near interfaces, creating stress concentration. When the stress value exceeds the alloy strength, there are lots of cracks along the grain boundaries, causing fracture. For practical applications it is necessary to stay away from this domain and corresponding processing parameters. The domain C occurs at high temperature and very low strain rate.

In this instability region many research results indicate that the DRX grains are coarsened and the hot workability of the alloy in this region is inferior [28]. Hot working in this region is also considered to be unsafe. Therefore, by means of the modified processing map developed in Fig. 6, the optimized conditions for hot deformation of the Cu-Cr-Zr-Y alloy can be proposed at the temperature range of 800–850 °C and the strain rate range of 0.01–1 s^{-1} .

3.4. Microstructure evolution

Optical images of the Cu-Cr-Zr-Y alloy microstructure deformed at 0.5 strain and different deformation conditions are shown in Fig. 7. The original grains are elongated vertically with respect to the compression direction when deformed at 650 °C and 0.1 s^{-1} strain rate, as seen in Fig. 7(a). There are no obvious recrystallized grains observed, except for the shear zone in Fig. 7(b). As the deformation temperature increased, the incomplete recrystallized structure formed along the grain boundaries in Fig. 7(c). The serrated grain boundaries marked by the arrows and some small DRX grains were observed in Fig. 7(d). This indicated the occurrence of initial recrystallized grains [29]. This microstructure has similar characteristics with the mixed-grain microstructure. Under these deformation conditions, corresponding with the processing maps in Fig. 6, the alloy is unstable. This means that the instability mechanisms are associated with cracking, localized plastic flow or adiabatic shear bands at low temperature and high strain rate in the domain B [30]. Therefore, the alloy can easily fracture during deformation processing. Thus, these deformation conditions and corresponding microstructure should be avoided in industrial practice. With the increasing temperature, the specimen deformed in the domain A exhibits completed DRX structure in Fig. 7(e). According to Fig. 7(e), the original grains were replaced entirely by the new DRX grains when the alloy was deformed at 850 °C and 0.1 s^{-1} . Typical recrystallization with uniform and fine grains was observed in Fig. 7(e). This means that the full DRX has been achieved. Subsequently, the recrystallized grains enlarged, as seen in Fig. 7(f). Comparing Fig. 7(e) and (f), the DRX grains deformed at 850 °C and 0.001 s^{-1} obviously grow in size, but the DRX grains are still fine and homogeneous. Deformed at high temperature and low strain rate, the DRX grains have larger driving force for nucleation and growth [31]. Therefore, it can be concluded that the deformation temperature and strain rate can strongly affect the deformed microstructure. The optimal processing parameters for hot deformation of the Cu-Cr-Zr-Y alloy are: temperature range of 800–850 °C and strain rate range of 0.01–1 s^{-1} .

Fig. 8 shows TEM micrographs of the Cu-Cr-Zr-Y alloy deformed at various deformation conditions. Elongated narrow structures were observed at low temperature and high strain rate, as seen in Fig. 8(a). The tangled dislocation walls and tiny dislocation sliding bands can be found. Dislocations are tangled and stored in the grains interior of the Cu-Cr-Zr-Y alloy deformed at 750 °C with the 0.1 s^{-1} strain rate, shown in Fig. 8(b). Due to relatively low stored energy by plastic deformation, there are no dynamic recrystallization grains observed at low deformation temperature and high strain rate. Therefore, dynamic recovery is the main softening mechanism. Dynamic recrystallization often appears at high temperature and low strain rate [32] because there is enough time to store energy. When the stored energy reaches a critical value, dynamic recrystallization occurs. Precipitation of the secondary phases also influences dynamic recrystallization characteristics [33]. TEM images of the precipitates are shown in Fig. 8(c). The selected area electron diffraction (SAED) pattern is shown in Fig. 8(d). It indicates that the precipitates are chromium-rich particles. The nucleation of dynamically recrystallized grains appears at the high-angle grain boundaries marked by an arrow in

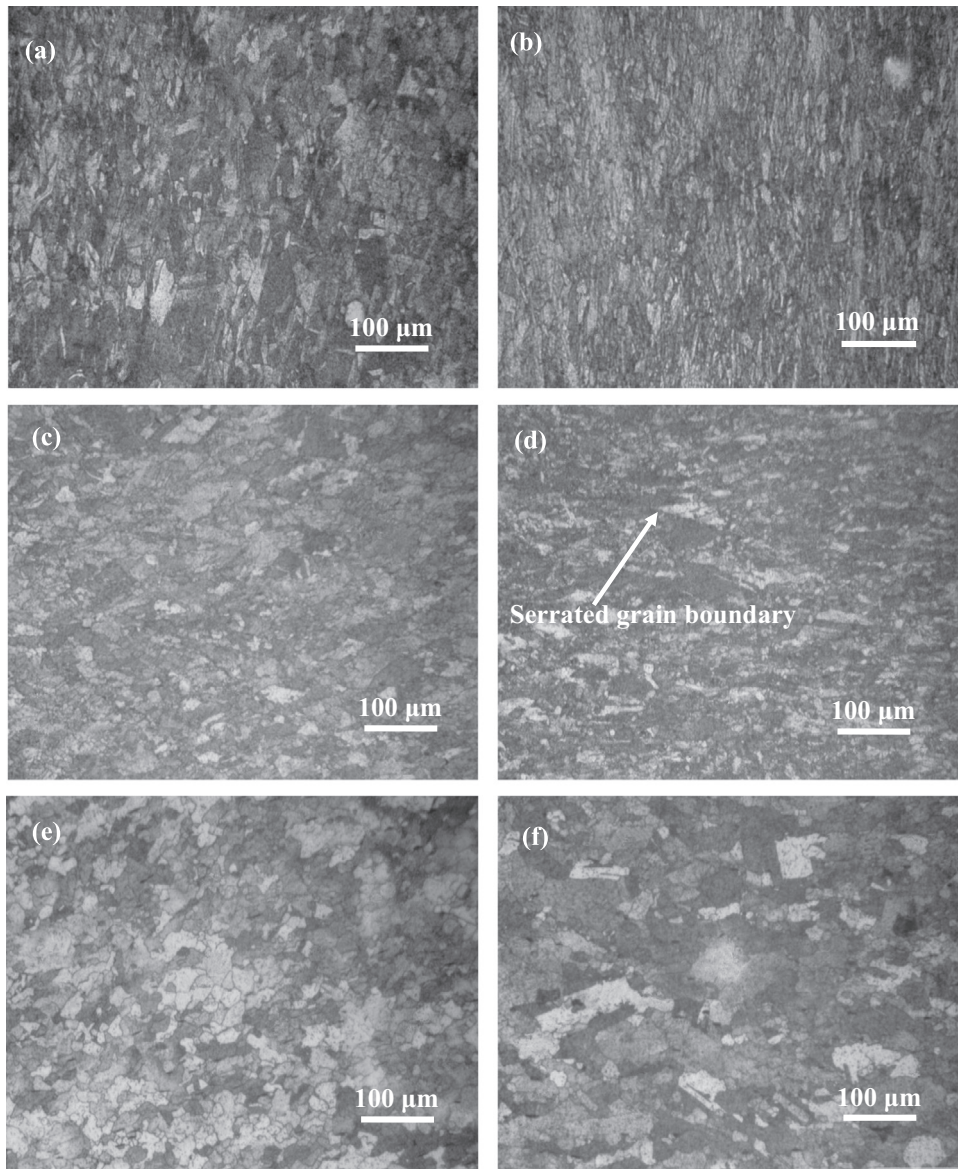


Fig. 7. Optical images of the microstructure of the hot compressed specimens deformed to 0.5 strain and different conditions: (a) 650 °C, 0.1 s⁻¹; (b) 700 °C, 0.1 s⁻¹; (c) 750 °C, 0.001 s⁻¹; (d) 800 °C, 1 s⁻¹; (e) 850 °C, 0.1 s⁻¹ and (f) 850 °C, 0.001 s⁻¹.

Fig. 8(e). It can be seen that the DRX grains grew up when the alloy was deformed at high temperature and low strain rate.

4. Discussion

4.1. Y effects on processing maps

Processing maps constructed for the Cu-Cr-Zr and Cu-Cr-Zr-Y alloys at a true strain of 0.4 are shown in Fig. 9(a) and (b), respectively. The processing map for the base Cu-Cr-Zr alloy in Fig. 9(a) exhibits a stable domain in the 800–850 °C temperature and 0.01–1 s⁻¹ strain rate ranges with a peak efficiency of about 47% at 850 °C and 0.1 s⁻¹ in the domain A marked by the red circle. The processing map for the Cu-Cr-Zr-Y alloy from Fig. 9(b) has a similar stable domain as the base Cu-Cr-Zr alloy in Fig. 9(a) with a peak efficiency of about 48% at 850 °C and 0.1 s⁻¹ in the domain A marked by the red circle. Comparing the two domains, the peak efficiency increased by 2% because of the Y addition. According to Fig. 9(b), it also can be seen that the spacing between the contour

lines becomes much closer in the domain A. This means that the Cu-Cr-Zr-Y alloy has much higher efficiency of energy dissipation (η) at the same deformation conditions. The η increased by 9% because of the Y addition, while the two alloys deformed at 800 °C and 0.1 s⁻¹ in the domain A marked by red square. Much higher η value means better hot workability of Cu-Cr-Zr-Y alloy. It also means that the addition of Y can improve the hot workability of the Cu-Cr-Zr alloy. The processing maps of both Cu-Cr-Zr and Cu-Cr-Zr-Y alloys have similar instability regimes at high temperature and very low strain rate (domain B), while coarsen DRX grains are often found at these regimes. The processing maps of both Cu-Cr-Zr and Cu-Cr-Zr-Y alloys show wide instability regimes at high strain rates, marked as domains C and D in the maps, which are also similar to each other. Many research results show that flow instability leads to adiabatic shear band formation at high strain rates [34]. Thus, these flow instability regimes should be avoided during hot processing. The domains of the maps are interpreted based on the efficiency variation associated with microstructure changes [35]. Corresponding microstructure in different domains of the processing maps will be compared next for the two alloys.

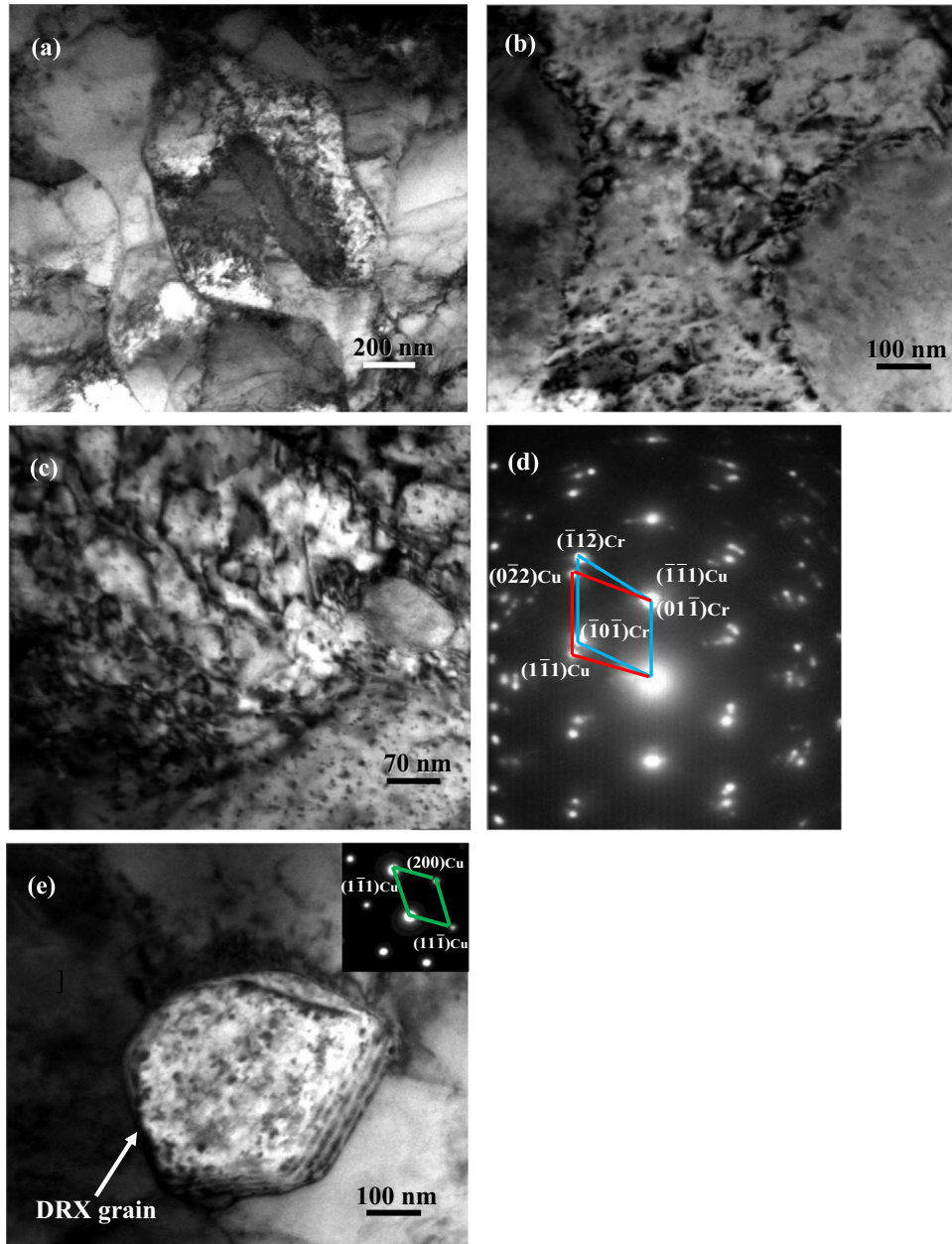


Fig. 8. TEM micrographs of the Cu-Cr-Zr-Y alloy deformed at: (a) 650 °C and 10 s^{-1} ; (b) 750 °C and 0.1 s^{-1} ; (c) 800 °C and 0.001 s^{-1} ; (d) SAED pattern for (c); (e) 850 °C and 0.1 s^{-1} .

4.2. Y effects on microstructure

Fig. 10 (a) and (b) show the microstructure of the Cu-Cr-Zr and Cu-Cr-Zr-Y alloys after solution treatment, where Y addition evidently refined the grain. Domain C is common in the processing maps of the two alloys. Microstructure of the specimens deformed at 650 °C and 10 s^{-1} (marked by the diamond in Fig. 9) is shown in Fig. 11 (a) and (c), respectively. It can be seen that there is only shear zone present with no dynamic recrystallization grains found. This means that the main softening mechanism is dynamic recovery in the domain C. Comparing Fig. 11 (a) and (c), much smaller grains are observed for the Cu-Cr-Zr-Y alloy. According to Fig. 11 (b), the DRX grains nucleated at the initial grain boundaries with deformation bands. This structure is often called typical necklace-type structure by some researchers [36]. Such observations suggest that DRX occurs in this domain. From Fig. 11 (d), the

Cu-Cr-Zr-Y alloy deformed at the same conditions compared with the Cu-Cr-Zr alloy, the shear bands has become unclear and a large number of smaller DRX grains were obtained. This means that the addition of Y can effectively refine the grain and improve dynamic recrystallization. However, the microstructure at these deformation conditions has mixed small dynamic recrystallized and elongated grains. In practical applications, these deformation conditions are recognized as unstable and unsafe, and should be avoided.

The Cu-Cr-Zr and Cu-Cr-Zr-Y alloys deformed in the domain A exhibit DRX structure in Fig. 12. The domain A occurs at lower strain rates and higher temperatures, and has the highest efficiency. Microstructure in Fig. 12(b) and (d) corresponds to the peak efficiency conditions in the domain A for the two alloys, respectively. According to Fig. 12(a), some elongated initial grains are still observed in the Cu-Cr-Zr alloy. This also means that hot deformation at these conditions is unsafe. With the increasing

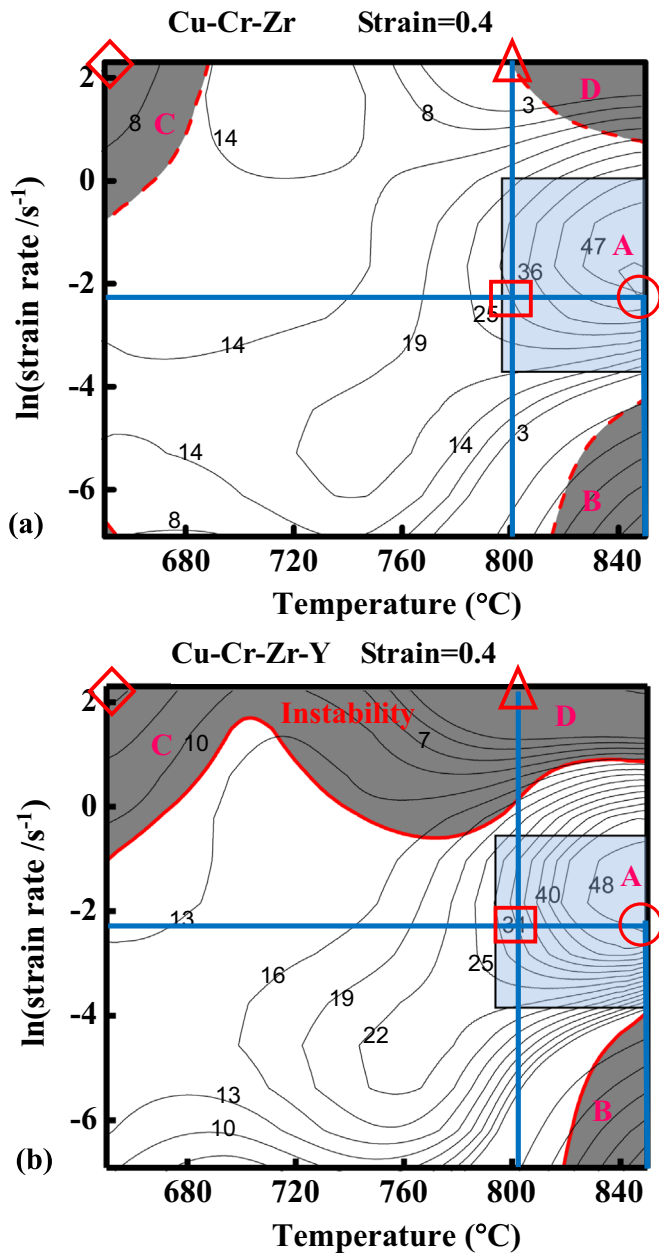


Fig. 9. Processing maps of (a) Cu-Cr-Zr alloy and (b) Cu-Cr-Zr-Y alloy at 0.4 true strain.

temperature, small coarsened DRX grains are obtained in Fig. 12 (b). The coarsening of the DRX grains also means instability during hot deformation. Complete recrystallization with uniform and fine grains is observed in Fig. 12(c) and (d). Comparing the two alloys, the DRX grain size of the Cu-Cr-Zr-Y alloy is smaller and more uniform than the Cu-Cr-Zr alloy deformed at the same conditions. It shows again that the addition of Y can refine the grain and improve dynamic recrystallization. The reason for this is because the DRX nucleation is improved by the increases boundaries area, since the grain size is refined by the addition of Y. The boundary movement and grain rotation can be promoted because of the fine recrystallized grains during hot deformation [37]. Thus, a mass of dislocations pile up during hot deformation. The microstructure the Cu-Cr-Zr and Cu-Cr-Zr-Y alloys deformed at 800 °C and 1 s⁻¹ is shown in Fig. 13(a) and (b), respectively. Comparing the two alloys, the addition of Y can increase the formation of dislocation density at the same deformation conditions. The amount of accumulated energy was increased with the increasing dislocation density due to Y addition. Finally, the driving force for recrystallized nucleation was improved with the existence of accumulated energy and dislocations.

5. Conclusions

Hot deformation behavior of Cu-Cr-Zr-Y alloy has been investigated in the 650–850 °C temperature range and 0.001–10 s⁻¹ strain rate range. Based on the obtained experimental and modeling results, the following conclusions can be drawn:

- (1) The flow stress increases with the strain rate and stress decreases with the deformation temperature.
- (2) The apparent activation energy for hot deformation of Cu-Cr-Zr-Y alloy is 336 kJ/mol. The constitutive equation for the flow stress can be expressed as: $\dot{\epsilon} = 1.723 \times 10^{14} [\sinh(0.0143\sigma)]^{7.122} \exp(-335.99/RT)$.
- (3) The processing maps at 0.3, 0.4 and 0.5 strain were established based on the DMM principles. The optimal processing parameters for hot deformation of the Cu-Cr-Zr-Y alloy were obtained through the processing maps: 800–850 °C temperature range and 0.01–1 s⁻¹ strain rate range.
- (4) The evolution of DRX microstructure strongly depends on the deformation conditions (temperature and strain rate). The dynamic recovery is the main softening mechanism at low temperature and high strain rate. Dynamic recrystallization appears at high temperature and low strain rate. The precipitates of chromium-rich particles were observed during hot deformation. The addition of Y can refine the grain and effectively accelerate dynamic recrystallization.

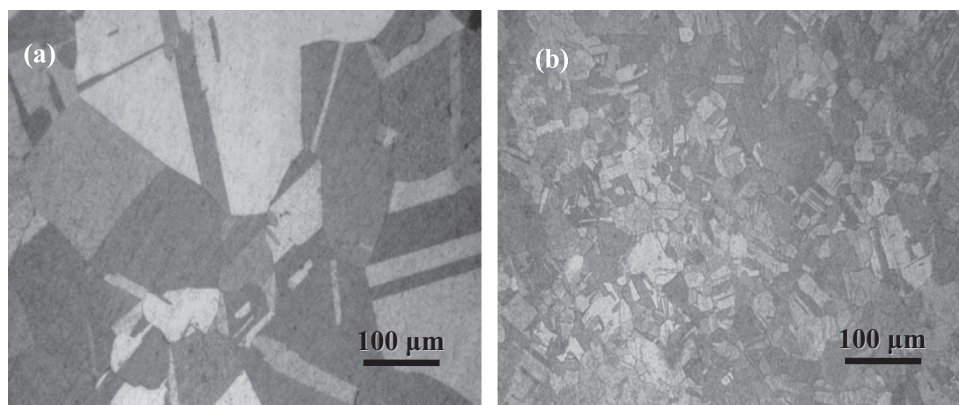


Fig. 10. Microstructure of (a) Cu-Cr-Zr and (b) Cu-Cr-Zr-Y alloys after solution treatment at 900 °C for 1 h.

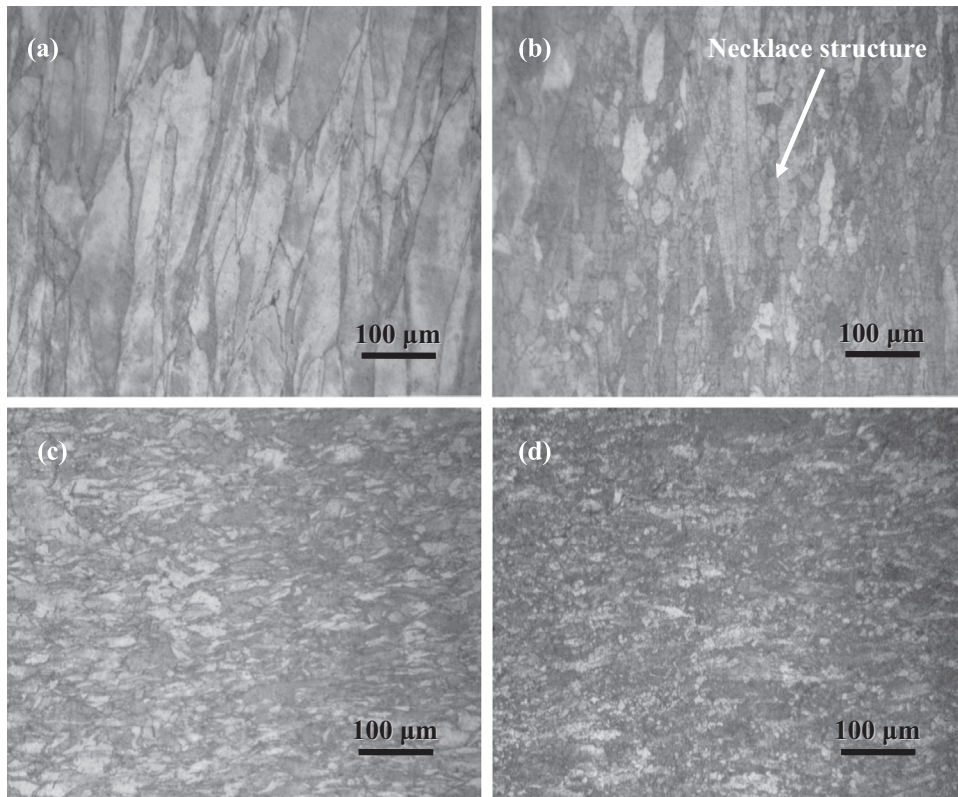


Fig. 11. Microstructure of (a–b) Cu-Cr-Zr and (c–d) Cu-Cr-Zr-Y alloys hot deformed in domains C and D: (a) 650 °C and 10 s^{-1} ; (b) 800 °C and 10 s^{-1} ; (c) 650 °C and 10 s^{-1} ; (d) 800 °C and 10 s^{-1} .

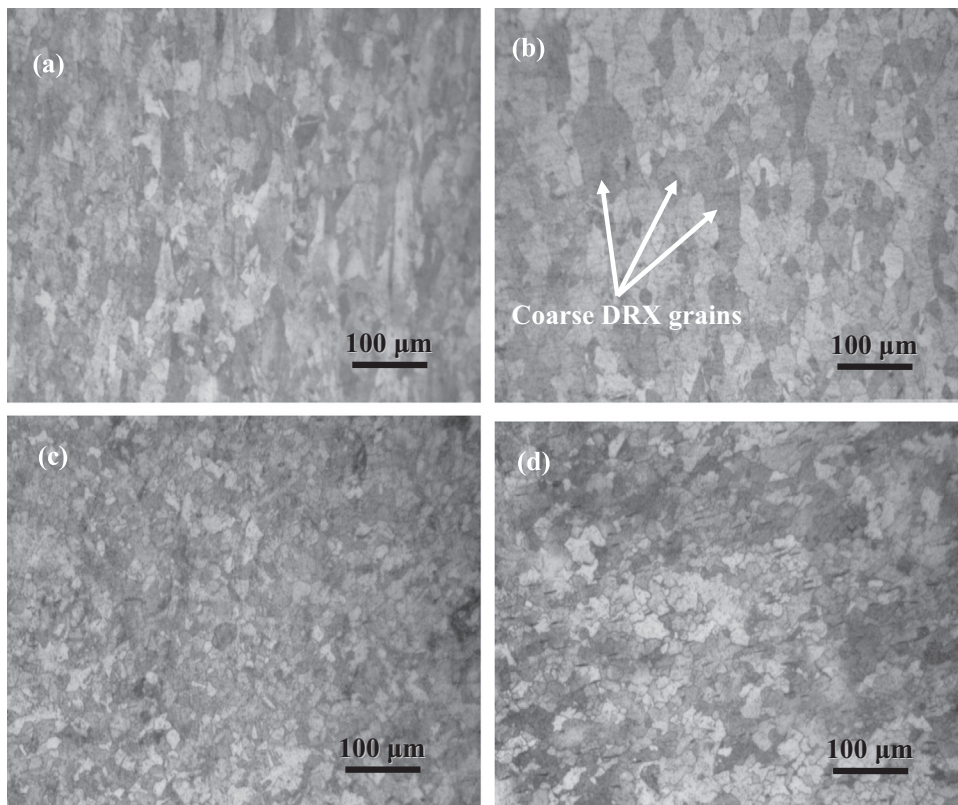


Fig. 12. Optical microstructures of (a–b) Cu-Cr-Zr and (c–d) Cu-Cr-Zr-Y alloys deformed at domain A: (a) 800 °C and 0.1 s^{-1} ; (b) 840 °C and 0.1 s^{-1} ; (c) 800 °C and 0.1 s^{-1} ; (d) 840 °C and 0.1 s^{-1} .

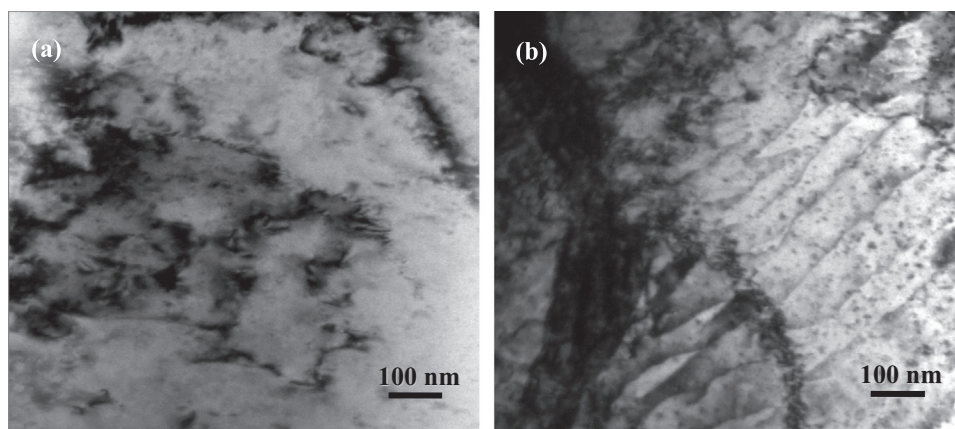


Fig. 13. TEM micrographs of the (a) Cu-Cr-Zr and (b) Cu-Cr-Zr-Y alloys deformed at 800 °C and 1 s^{-1} .

Acknowledgements

This work was supported by the National Natural Science Foundation of China (51101052) and the National Science Foundation (IRES 1358088).

References

- [1] J.H. Su, Q.M. Dong, P. Liu, H.J. Li, B.X. Kang, *Mater. Sci. Eng. A* 392 (2005) 422–426.
- [2] P. Liu, B.X. Kang, X.G. Cao, J.L. Huang, B. Yen, H.C. Gu, *Mater. Sci. Eng. A* 265 (1999) 262–267.
- [3] S. Chenna Krishna, N.K. Gangwar, A.K. Jha, B. Pant, K.M. George, *J. Mater. Eng. Perform.* 23 (2014) 1458–1464.
- [4] G.B. Lin, Z.D. Wang, M.K. Zhang, H. Zhang, M. Zhao, *Mater. Sci. Technol.* 27 (2011) 966–969.
- [5] L.M. Bi, P. Liu, X.H. Chen, X.K. Liu, W. Li, F.C. Ma, *Trans. Nonferrous Met. Soc. China* 23 (2013) 1342–1348.
- [6] Y.Q. Long, P. Liu, Y. Liu, W.M. Zhang, J.S. Pan, *Mater. Lett.* 62 (17–18) (2008) 3039–3042.
- [7] L. Zhang, Z. Li, Q. Lei, W.T. Qiu, H.T. Luo, *Mater. Sci. Eng., A* 528 (2011) 1641–1647.
- [8] Y. Zhang, A.A. Volinsky, H.T. Tran, Z. Chai, P. Liu, B.H. Tian, *J. Mater. Eng. Perform.* 24 (2015) 3783–3788.
- [9] H. Zhang, H.G. Zhang, L.X. Li, *J. Mater. Process. Technol.* 209 (2009) 2892–2896.
- [10] D.G. Cram, H.S. Zuro, Y.J.M. Brechet, C.R. Hutchinson, *Acta Mater.* 57 (2009) 5218–5228.
- [11] A. Etaati, K. Dehghani, *Mater. Chem. Phys.* 140 (2013) 208–215.
- [12] M.H. Wang, Y.F. Li, W.H. Wang, J. Zhou, Akihiko Chiba, *Mater. Des.* 45 (2013) 384–392.
- [13] S.M. Abbasi, A. Shokuhfar, *Mater. Lett.* 61 (2007) 2523–2526.
- [14] A. Galiyev, R. Kaibyshev, G. Gottstein, *Acta Mater.* 49 (2001) 1199–1207.
- [15] E.X. Pu, W.J. Zheng, J.Z. Xiang, Z.G. Song, J. Li, *Mater. Sci. Eng. A* 598 (2014) 174–182.
- [16] C.M. Sellars, W.J. Mctegart, *Acta Metall.* 14 (1966) 1136–1138.
- [17] C. Zener, J.H. Hollomon, *J. Appl. Phys.* 15 (1944) 22–32.
- [18] Z.Y. Ding, S.G. Jia, P.F. Zhao, M. Deng, K.X. Song, *Mater. Sci. Eng. A* 570 (2013) 87–91.
- [19] G.L. Ji, Q. Li, K.Y. Ding, L. Yang, L. Li, *J. Alloys Compd.* 648 (2015) 397–407.
- [20] Y.V.R.K. Prasad, T. Seshacharyulu, *Mater. Sci. Eng. A* 243 (1998) 82–88.
- [21] H.Z. Zhao, L. Xiao, P. Ge, J. Sun, Z.P. Xi, *Mater. Sci. Eng. A* 604 (2014) 111–116.
- [22] X.S. Xia, Q. Chen, K. Zhang, Z.D. Zhao, M.L. Ma, X.G. Li, Y.J. Li, *Mater. Sci. Eng. A* 587 (2013) 283–290.
- [23] L. Wang, F. Liu, J.J. Cheng, Q. Zuo, C.F. Chen, *J. Alloys Compd.* 623 (2015) 69–78.
- [24] T.D. Kil, J.M. Lee, Y.H. Moon, *J. Mater. Process. Technol.* 220 (2015) 224–230.
- [25] T. Xi, C.G. Yang, M.B. Shahzad, K. Yang, *Mater. Des.* 87 (2015) 303–312.
- [26] Q.L. Pan, B. Li, Y. Wang, Y.W. Zhang, Z.M. Yin, *Mater. Sci. Eng. A* 585 (2013) 371–378.
- [27] H. Mirzadeh, *J. Mater. Eng. Perform.* 24 (2015) 1095–1099.
- [28] L. Wang, F. Liu, J.J. Cheng, Q. Zuo, C.F. Chen, *J. Alloys Compd.* 623 (2015) 69–78.
- [29] D.J. Li, Y.R. Feng, Z.F. Yin, F.S. Shangguan, K. Wang, Q. Liu, F. Hu, *Mater. Sci. Eng. A* 528 (2011) 8084–8089.
- [30] Y. Sun, W.D. Zeng, Y.Q. Zhao, X.M. Zhang, Y. Shu, Y.G. Zhou, *Mater. Sci. Eng. A* 528 (2011) 1205–1211.
- [31] A. Momeni, S. Abbasi, M. Morakabati, H. Badri, X. Wang, *Mater. Sci. Eng. A* 615 (2014) 51–60.
- [32] Y.G. Kim, S.H. Lee, S. Lee, J.W. Noh, *Mater. Sci. Eng. A* 552 (2012) 276–282.
- [33] H. Yin, H.Y. Li, X.J. Su, D.S. Huang, *Mater. Sci. Eng. A* 586 (2013) 115–122.
- [34] D.X. Wen, Y.C. Lin, J. Chen, X.M. Chen, J.L. Zhang, Y.J. Liang, *J. Alloys Compd.* 618 (2015) 372–379.
- [35] C. Dharmendra, K.P. Rao, F. Zhao, Y.V.R.K. Prasad, N. Hort, K.U. Kainer, *J. Mater. Sci.* 49 (2014) 5885–5898.
- [36] S.L. Semiatin, D.S. Weave, R.C. Kram, P.N. Fagin, M.G. Glavicic, R.L. Goetz, N. D. Frey, M.M. Antony, *Met. Mater. Trans. A* 35A (2004) 679–693.
- [37] Y.Y. Chen, B.H. Li, F.T. Kong, *T. Nonferrous Metal. Soc.* 17 (2007) 58–63.